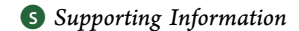




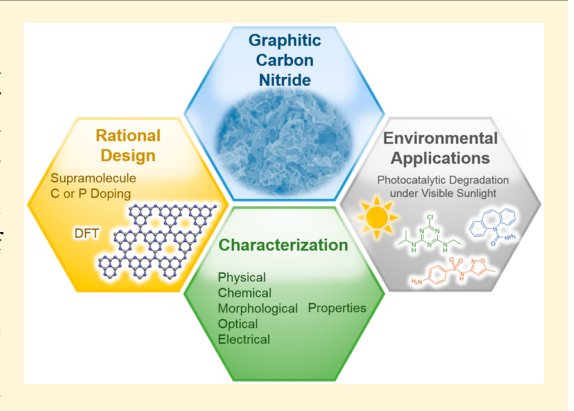
# Visible-Light-Responsive Graphitic Carbon Nitride: Rational Design and Photocatalytic Applications for Water Treatment

Qinmin Zheng, David P. Durkin, Justin E. Elenewski, Yingxue Sun, Nathan A. Banek, Likun Hua, Hanning Chen, Michael J. Wagner, Wen Zhang, on Danmeng Shuai\*, †

 $<sup>^{\</sup>perp}$ Department of Civil and Environmental Engineering, New Jersey Institute of Technology, Newark, New Jersey 07102, United States



ABSTRACT: Graphitic carbon nitride (g-C<sub>3</sub>N<sub>4</sub>) has recently emerged as a promising visible-light-responsive polymeric photocatalyst; however, a molecular-level understanding of material properties and its application for water purification were underexplored. In this study, we rationally designed nonmetal doped, supramolecule-based g-C<sub>3</sub>N<sub>4</sub> with improved surface area and charge separation. Density functional theory (DFT) simulations indicated that carbon-doped g-C<sub>3</sub>N<sub>4</sub> showed a thermodynamically stable structure, promoted charge separation, and had suitable energy levels of conduction and valence bands for photocatalytic oxidation compared to phosphorus-doped g-C<sub>3</sub>N<sub>4</sub>. The optimized carbon-doped, supramoleculebased g-C<sub>3</sub>N<sub>4</sub> showed a reaction rate enhancement of 2.3–10.5-fold for the degradation of phenol and persistent organic micropollutants compared to that of conventional, melamine-based g-C<sub>3</sub>N<sub>4</sub> in a model buffer system under the irradiation of simulated visible sunlight. Carbon-doping but not



phosphorus-doping improved reactivity for contaminant degradation in agreement with DFT simulation results. Selective contaminant degradation was observed on g-C<sub>3</sub>N<sub>4</sub>, likely due to differences in reactive oxygen species production and/or contaminant-photocatalyst interfacial interactions on different g-C<sub>3</sub>N<sub>4</sub> samples. Moreover, g-C<sub>3</sub>N<sub>4</sub> is a robust photocatalyst for contaminant degradation in raw natural water and (partially) treated water and wastewater. In summary, DFT simulations are a viable tool to predict photocatalyst properties and oxidation performance for contaminant removal, and they guide the rational design, fabrication, and implementation of visible-light-responsive g-C<sub>3</sub>N<sub>4</sub> for efficient, robust, and sustainable water treatment.

## ■ INTRODUCTION

A growing number of persistent organic micropollutants such as pharmaceuticals and personal care products (PPCPs), endocrine disrupting compounds (EDCs), pesticides, and herbicides are frequently observed in natural and treated water. 1,2 These contaminants are recalcitrant to conventional water and wastewater treatment<sup>3</sup> and may pose risks to human and ecological systems even at very low concentrations.<sup>4</sup> Photocatalysis is a promising advanced oxidation process (AOP) for the degradation or mineralization of persistent organic micropollutants because it activates O<sub>2</sub> and/or H<sub>2</sub>O at ambient conditions to generate reactive oxygen species (ROS, e.g., OH,  $O_2^-$ ·/HO<sub>2</sub>·,  $H_2O_2$ ,  $^1O_2$ ) in situ. <sup>5,6</sup> Photocatalysis also eliminates the hurdles in the storage, handling, and transportation of oxidants and potentially uses renewable solar energy for water purification.

Visible-light-responsive photocatalysts attract great attention because they can harvest and potentially utilize more sunlight for reactions (visible light constitutes 40% of solar energy) than

conventional photocatalysts (e.g., titanium dioxide, TiO<sub>2</sub>) and can be reactive under artificial light. A number of visible-lightresponsive photocatalysts were synthesized and used for lab scale water treatment studies, such as metal or nonmetal doped TiO<sub>2</sub>,<sup>8</sup> metal doped tungsten trioxide,<sup>9</sup> silver phosphate,<sup>10</sup> bismuth vanadate, 11 bismuth oxyhalides, 12 metal chalcogenides, 13,14 and upconversion materials. 15 Nevertheless, these materials may suffer from low photocatalytic activity (due to a low surface area or fast charge recombination), limited photostability (e.g., photocorrosion of chalcogenides), release of toxic chemicals (e.g., Cd2+ leaching from CdS), and potentially high cost for fabrication (e.g., the use of noble metals). These issues largely limit practical engineering

May 23, 2016 Received: Revised: October 31, 2016 Accepted: November 4, 2016 Published: November 4, 2016

Department of Civil and Environmental Engineering, The George Washington University, Washington, DC 20052, United States

<sup>\*</sup>Department of Chemistry, Johns Hopkins University, Baltimore, Maryland 21218, United States

<sup>§</sup>Department of Chemistry, The George Washington University, Washington, DC 20052, United States

Department of Environmental Science and Engineering, Beijing Technology and Business University, Beijing 100048, China

**Environmental Science & Technology** 

Scheme 1. Synthesis Schematic of (a) Carbon-Doped and (b) Phosphorus-Doped Supramolecule-Based g-C<sub>2</sub>N<sub>4</sub><sup>a</sup>

"In addition to MCB, and MCE, MC was also synthesized via the supramolecular approach by thermal polycondensation of melamine and cyanuric acid. Details of g-C<sub>3</sub>N<sub>4</sub> synthesis are included in the Experimental Section. C or P represents the possible sites for carbon or phosphorus doping based on DFT simulations.

applications of visible-light-responsive photocatalysts for water purification.  $^{8,10,14-16}$ 

Recently, graphitic carbon nitride (g-C<sub>3</sub>N<sub>4</sub>) has emerged as an innovative photocatalyst with tunable band gaps of 1.8-2.7 eV that allow the harvesting of visible light up to 460-698 nm (potentially utilizing 13-49% of solar energy, though photocatalytic activity may be reduced at a longer wavelength). 17-19 This material is made from earth-abundant, inexpensive C and N containing precursors (e.g., urea and melamine), is biocompatible with no reported toxicity, is resistant to photocorrosion, and remains chemically stable in harsh environments.  $^{20-23}$  However, the application of g-C<sub>3</sub>N<sub>4</sub> in environmental remediation is at its nascent stage. A few studies reported that g-C<sub>3</sub>N<sub>4</sub> held promise for the oxidation of organic dyes and the inactivation of microorganisms, 24-33 but all of them were focused on the degradation of model contaminants in simple water chemistry that has limited environmental relevance. There are no reports about the degradation of persistent organic micropollutants on g-C<sub>3</sub>N<sub>4</sub> in complex water matrixes that are representative of treatment operations in practice. Photocatalytic performance on g-C<sub>3</sub>N<sub>4</sub> may also be challenged by a low surface area, fast recombination of charge carriers (i.e., electrons and holes), and limited visible-light utilization, 24-27 which demands more work to tailor the photocatalyst properties for effective water purification.

Supramolecular preassembly of triazine precursors has become an attractive approach to tailor the properties and reactivity of  $g-C_3N_4$ . The supramolecular approach is more environmentally benign and sustainable compared to widely used hard-templating with nanosilica because no toxic or corrosive chemicals are involved (e.g., HF or NH<sub>4</sub>HF<sub>2</sub> for the postremoval of silica and pore generation). 40,41 Cyanuric acid was widely applied with melamine because they can interact with each other by forming hydrogen bonds, producing a highly stable aggregate as the precursor of g- $C_3N_4$ .  $^{26,34-39}$  Cyanuric acid is less thermally stable than melamine and decomposed into gases at an elevated temperature, which may create a porous structure of g- $C_3N_4$  with an increased surface area and charge separation. The molecular structure of g- $C_3N_4$  has also been tailored with metal dopants, 45-47 nonmetal dopants, 48-51 or nanoparticles 52-54 to improve charge separation and visible-light utilization. We selected earthabundant, low-cost, nontoxic dopants, i.e., carbon and phosphorus, because metal dopants or nanoparticles are more expensive (e.g., noble metal loading)<sup>52–54</sup> and may leach or be deactivated in complex aquatic chemistries (e.g., metals fouled by natural organic matter, NOM, or sulfide). 55,56 Barbituric acid or etidronic acid was used for carbon or phosphorus doping because it can be incorporated into the supramolecular complex **Environmental Science & Technology** 

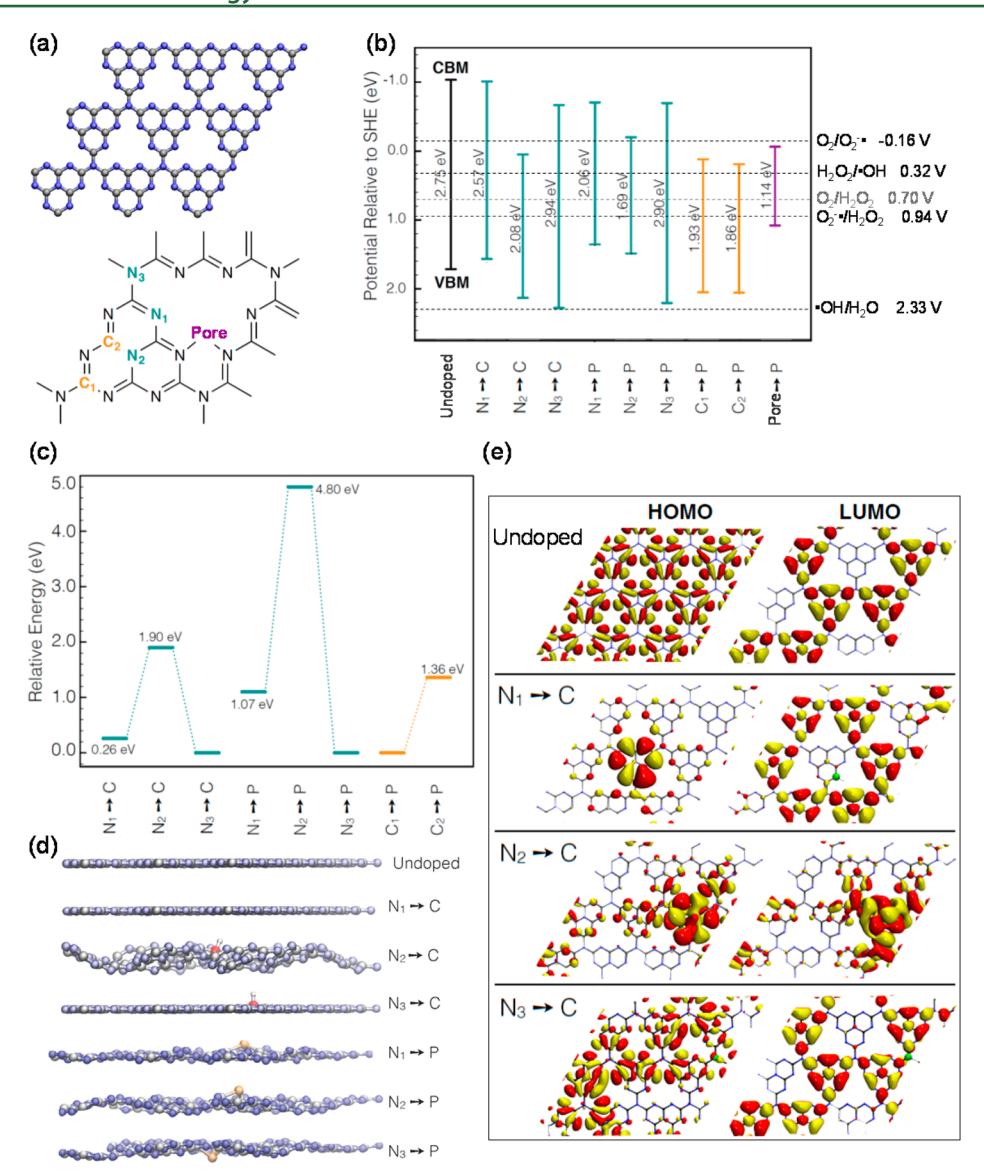


Figure 1. (a) Undoped g- $C_3N_4$  sheet employed in electronic structure calculations and designated sites for doping (i.e.,  $N_1$ ,  $N_2$ ,  $N_3$ ,  $C_1$ ,  $C_2$  and Pore). (b) Band gap, VBM, and CBM of undoped and doped g- $C_3N_4$ , determined with respect to the SHE. Redox potentials of ROS production are also included for comparison. (c) Relative stability of doped g- $C_3N_4$  with respect to the most stable member of each family (i.e., carbon-doped g- $C_3N_4$ , phosphorus-doped g- $C_3N_4$  for carbon sites, and phosphorus-doped g- $C_3N_4$  for nitrogen sites). The stability is compared only within each dopant family, as the zero energy reference point differs for each doping pattern. (d) Optimized geometry of undoped and doped g- $C_3N_4$ ; the dopant atom is highlighted in red or yellow. (d) HOMO and LUMO of undoped and carbon-doped g- $C_3N_4$ .

of melamine and cyanuric acid via hydrogen bonding or electrostatic interactions to promote efficient doping. 35,38,57,58

In this work, instead of trial-and-error material development by an Edisonian approach, we applied density functional theory (DFT) simulations as a guide to rationally design the doped supramolecule-based g-C<sub>3</sub>N<sub>4</sub> with an improved photocatalytic activity for the degradation of persistent organic micropollutants. First, the molecular structure, band gap, band energy levels, and charge separation of carbon- and phosphorus-doped g-C<sub>3</sub>N<sub>4</sub> were evaluated by DFT simulations, which provide the mechanistic understanding of photocatalyst properties and the prediction of photocatalytic activity for contaminant removal. In contrast to the previous DFT simulations which only investigate the effect of carbon or phosphorus doping on limited possible positions of g-C<sub>3</sub>N<sub>4</sub> structure, <sup>51,59,60</sup> we evaluated g-C<sub>3</sub>N<sub>4</sub> properties and stability of any possible doped structure (see Results and Discussion) and

compared the calculated band energy with ROS redox potentials to determine the thermodynamic feasibility of photocatalytic reactions on the doped g-C<sub>3</sub>N<sub>4</sub>. Next, we synthesized doped supramolecule-based g-C<sub>3</sub>N<sub>4</sub> by the thermal polymerization of melamine-cyanuric acid-barbituric acid (or etidronic acid) complexes (Scheme 1). 26,38,44 As indicated in a comprehensive review, 42 similar carbon or phosphorus doping was also reported for supramolecule-based g-C<sub>3</sub>N<sub>4</sub>, but different solvents (water vs ethanol), precursors for doping (inorganic phosphoric acid vs organic etidronic acid), or experimental procedures for synthesizing the supramolecular complexes resulted in g-C<sub>3</sub>N<sub>4</sub> with distinct structures in contrast to our study (see Results and Discussion).35,57 To the best of our knowledge, this is the first work that systematically applies DFT simulations as a guide to rationally design the doped g-C<sub>3</sub>N<sub>4</sub> with improved performance for the environmental application.

The photocatalytic performance of supramolecule-based g-C<sub>3</sub>N<sub>4</sub> and conventional g-C<sub>3</sub>N<sub>4</sub> fabricated from only melamine or urea was evaluated in batch suspensions under the irradiation of simulated visible sunlight ( $\lambda > 400$  nm), and the degradation kinetics of a model organic contaminant (i.e., phenol) and persistent organic micropollutants (i.e., atrazine, carbamazepine, and sulfamethoxazole) across a variety of water chemistries representative of drinking water and wastewater treatment was explored. Our study aims to identify the most influential properties of g-C<sub>3</sub>N<sub>4</sub> for the photocatalytic degradation of persistent organic micropollutants by the synergy of simulation and experimental approaches and evaluate the viability of g-C<sub>3</sub>N<sub>4</sub> for engineering applications in water treatment. The outcome of this work provides first insights into the guideline of photocatalytic g-C<sub>3</sub>N<sub>4</sub> design and lays the groundwork for the application of g-C<sub>3</sub>N<sub>4</sub> as an efficient, stable, low-cost visible-light-responsive photocatalyst toward more sustainable treatment of impaired water supplies.

#### EXPERIMENTAL SECTION

DFT Simulations. Electronic structure calculations were conducted using  $\mathrm{DFT}^{61,62}$  as implemented in the CP2K suite.  $^{6}$ 

Synthesis and Characterization of g-C<sub>3</sub>N<sub>4</sub>. Conventional g-C<sub>3</sub>N<sub>4</sub> samples, M and U, were prepared from the thermal polycondensation of melamine or urea, respectively. Under the same thermal treatment, the supramolecule-based g-C<sub>3</sub>N<sub>4</sub> sample without nonmetal doping, MC, was synthesized from melamine and cyanuric acid. Carbon- or phosphorusdoped supramolecule-based g-C<sub>3</sub>N<sub>4</sub> samples, MCB<sub>x</sub> or MCE<sub>y</sub> were synthesized from various mass ratios of melamine, cyanuric acid, and barbituric acid or etidronic acid, and x or yrepresents the mass of barbituric acid or etidronic acid, respectively. The physical, chemical, morphological, optical, and electronic properties of g-C<sub>3</sub>N<sub>4</sub> were characterized.

Photocatalytic Degradation of Contaminants. Photocatalytic experiments were conducted in batch reactors under a 1000 W xenon lamp equipped with a water optical filter to remove infrared light and a 400 nm long-pass optical filter ( $\lambda$  > 400 nm) to simulate the visible light in solar irradiation. The spectral irradiance and photon fluence of the xenon lamp were recorded by a spectroradiometer (Figure S1). Reactivity studies were conducted in a jacketed beaker with the presence of a contaminant (initial concentrations of 20 or 100  $\mu$ M), a phosphate buffer (pH 7.3, 1 mM), and a catalyst (1 g  $L^{-1}$ ) at 25 °C under magnetic stirring at 500 rpm. Any mass transfer limitations were eliminated under this well-mixed condition (details in the Supporting Information), and the observed reaction kinetics represents the intrinsic activity of g-C<sub>3</sub>N<sub>4</sub>. MCB<sub>x</sub> and MCE<sub>y</sub> synthesis was optimized using phenol and/or atrazine degradation as a performance indicator, and the doped g-C<sub>3</sub>N<sub>4</sub> with the highest reactivity (i.e., MCB<sub>0.07</sub>) was selected for the degradation of persistent organic micropollutants, including atrazine, carbamazepine, and sulfamethoxazole, which are known to be recalcitrant to traditional water and wastewater treatment.3 The concentration of contaminants collected at regular time intervals was analyzed by high performance liquid chromatography (HPLC). To explore the influence of water matrixes representative of water treatment systems, the reactivity of MCB<sub>0.07</sub> for atrazine degradation under xenon lamp irradiation ( $\lambda > 400$  nm) was explored in simulated water samples with complex constituents and in real water samples collected from the Griffith Water Treatment Plant (GWP) and the Broad Run Wastewater Reclamation Facility (BRWRF) in

Virginia. To understand the mechanism of the photocatalytic degradation on g-C<sub>3</sub>N<sub>4</sub>, we conducted phenol degradation on U with the presence of radical or hole scavengers under xenon lamp irradiation ( $\lambda > 400$  nm). tert-Butyl alcohol, superoxide dismutase, catalase, ammonium oxalate, and L-histidine were used to quench the reactions involved with the hydroxyl radical (·OH), superoxide anion radical  $(O_2^-)$ ,  $H_2O_2$ , hole, and  $^1O_2$ . Scavenger concentration was optimized to completely quench the reaction between the target radical and phenol/atrazine.

The pseudo-first-order rate constant for contaminant photocatalytic degradation was obtained by performing a linear regression of natural log of contaminant concentrations vs time. The reaction rate constants (with 95% confidence intervals) were reported with respect to the photon fluence, i.e., the pseudo-first-order rate constant divided by the photon fluence. Details of the experimental procedures are included in the Supporting Information.

#### RESULTS AND DISCUSSION

**DFT Simulations Predict Photocatalytic Performance** of Carbon or Phosphorus Doped g-C<sub>3</sub>N<sub>4</sub>. Our preliminary studies were performed on an undoped, HSE06-optimized (3 × 3) g-C<sub>3</sub>N<sub>4</sub> supercell (Figure 1a), revealing a planar geometry (Figure 1d) and a bandgap of 2.75 eV (Figure 1b). The conduction and valence band edges (-1.03 and 1.71 eV), measured with respect to the absolute potential of the standard hydrogen electrode (SHE; 4.44 eV), likewise lie near the experimentally determined values of -0.83 and 1.83 eV.64 Encouraged by the robust nature of these results, particularly with respect to prior theoretical studies, 60,65-68 we explored carbon and phosphorus doping at three inequivalent nitrogen sites (N<sub>1</sub>, N<sub>2</sub>, and N<sub>3</sub>), phosphorus substitution at inequivalent carbon atoms  $(C_1 \text{ and } C_2)$ , and the incorporation of phosphorus within the g-C<sub>3</sub>N<sub>4</sub> pore (i.e., interstitial doping), all with one dopant introduced to one doping site (Figure 1a). The doped materials are labeled as A  $\rightarrow$  B doped g-C<sub>3</sub>N<sub>4</sub> for further discussion (A is the doping site of  $N_1$ ,  $N_2$ ,  $N_3$ ,  $C_1$ ,  $C_2$ , and Pore, and B is the doping element of C or P).

To determine the thermodynamic ability of these materials to generate ROS and holes, we quantified their valence band maximum (VBM) and conduction band minimum (CBM) in conduction with an implicit solvation model, represented by the highest occupied molecular orbital (HOMO) and lowest unoccupied molecular orbital (LUMO) energies, respectively. As shown in Figure 1b (details in the Supporting Information), only  $N_{1,3} \to C$  and  $N_{1-3} \to P$  doped g- $C_3N_4$  can produce  $O_2^{-1}$ via one-electron reduction of O2 because their CBM is more negative than the redox potential of  $O_2/O_2^{-}$  ( $E^0(O_2/O_2^{-})$ ) = -0.16 V vs SHE). All doped materials are able to produce  $H_2O_2$  and  $\cdot OH$  from the one-electron reduction of  $O_2^{-} \cdot$  and  $H_2O_2$ , respectively  $(E^0(O_2^{-1}/H_2O_2) = 0.94 \text{ V} \text{ and } E^0(H_2O_2/\text{ C})$ OH) = 0.32 V vs SHE). However,  $O_2$  reduction for  $O_2^-$ . formation is the first step for ROS production on the conduction band (i.e., sequential reduction of  $O_2 \rightarrow O_2^- \rightarrow$  $H_2O_2 \rightarrow \cdot OH$ ), and those doped g-C<sub>3</sub>N<sub>4</sub> that cannot reduce O<sub>2</sub> may not produce sufficient ROS and thus result in low photocatalytic activity for contaminant degradation. Multielectron reduction could facilitate ROS production on the conduction band because it is more thermodynamically favorable than one-electron reduction  $(E^0(O_2/H_2O_2) = 0.70$ V vs SHE), but the loading of cocatalysts (e.g., Pt, Au, and Cu(II)) is always required. Recent studies have shown that g-C<sub>3</sub>N<sub>4</sub> in the form of nanosheets<sup>71</sup> or containing electron**Environmental Science & Technology** 

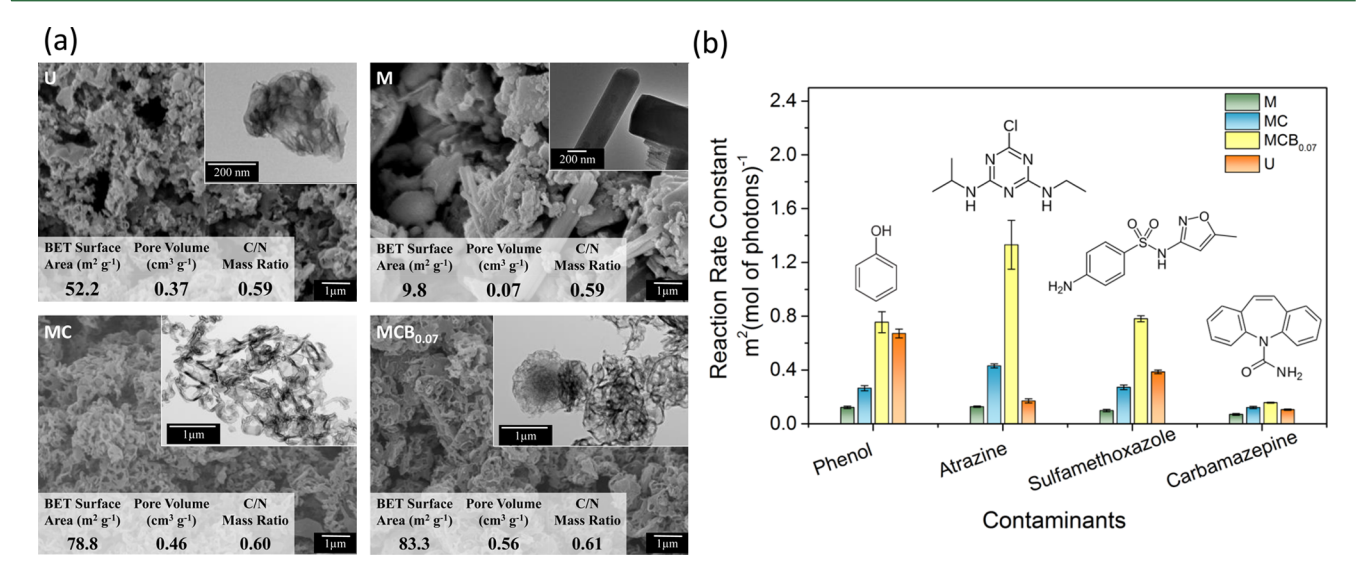


Figure 2. (a) SEM and TEM (insets) images of g-C<sub>3</sub>N<sub>4</sub> samples U, M, MC, and MCB<sub>0.07</sub>. Inset tables show the surface area, pore volume, and bulk carbon to nitrogen (C/N) mass ratio of each sample. (b) Photocatalytic degradation rate constants of phenol, atrazine, sulfamethoxazole, and carbamazepine on g- $C_3N_4$  (U, M, MC, and MCB<sub>0.07</sub>) under simulated visible sunlight irradiation ( $\lambda > 400$  nm, xenon lamp). The initial contaminant concentration was 100  $\mu$ M, and the reactions were conducted in a phosphate buffer (pH 7.3, 1 mM). Photocatalyst loading was 1 g L<sup>-1</sup>. Error bars represent 95% confidence intervals of replicates.

deficient aromatic diimide (as a cocatalyst)<sup>72</sup> can promote the multielectron photocatalytic reduction of O<sub>2</sub> for H<sub>2</sub>O<sub>2</sub>. None of the undoped or doped g-C<sub>3</sub>N<sub>4</sub> derivatives are able to oxidize water and produce ·OH on the valence band because the VBM is smaller than  $E^0(\cdot OH/H_2O)$  (2.33 V vs SHE). This suggests that g-C<sub>3</sub>N<sub>4</sub> oxidizes contaminants through a surface-localized hole that is generated from the valence band.  $N_{1,2} \rightarrow P$  and Pore → P doped g-C<sub>3</sub>N<sub>4</sub> have a lower-lying VBM and are expected to show low reactivity in photocatalytic oxidation. The band gap of  $N_3 \rightarrow C$  and  $N_3 \rightarrow P$  doped g-C<sub>3</sub>N<sub>4</sub> is larger than that of undoped g-C<sub>3</sub>N<sub>4</sub> (2.94 and 2.90 vs 2.75 eV), and these doped materials will only harvest and potentially utilize light with wavelengths shorter than 422 and 428 nm, respectively, resulting in low photocatalytic activity. The stability of doped g- $C_3N_4$  derivatives was also evaluated;  $N_{1,3} \rightarrow C$ ,  $N_3 \rightarrow P$ , and  $C_1$ → P doped g-C<sub>3</sub>N<sub>4</sub> were found to possess the most viable structure (with the lowest relative energy, Figure 1c). Our results are in agreement with previous experimental measurements, e.g., the structure of  $N_1 \rightarrow C$  and  $C_1 \rightarrow P$  doped g- $C_3N_4$ were confirmed by solid-state nuclear magnetic resonance spectroscopy. Previous simulations also suggested that interstitial doping by phosphorus (i.e., Pore  $\rightarrow$  P) might be thermodynamically stable; 60 however, the calculated redox properties of this material are expected to render it catalytically incompetent. Taken together, our DFT simulations predict that carbon-doped g- $C_3N_4$  ( $N_1 \rightarrow C$ ) will outperform phosphorusdoped g-C<sub>3</sub>N<sub>4</sub> for photocatalytic degradation of contaminants, as its band energy levels promote contaminant oxidation by both ROS and holes, a reduced band gap improves visible light utilization, and a thermodynamically stable structure is possessed.

As shown in Figure 1d, both  $N_1 \rightarrow C$  and  $N_3 \rightarrow C$  doped g-C<sub>3</sub>N<sub>4</sub> exhibit a planar geometry similar to that of undoped g- $C_3N_4$ . Conversely,  $N_2 \rightarrow C$  doped g- $C_3N_4$  is characterized by a significant out-of-plane deformation. The  $N_{1-3} \rightarrow P$  geometries are collectively more distorted, each exhibiting some degree of undulation due to the bulky phosphorus substituent, and are presumably less thermodynamically stable than their carbondoped counterparts due to strain. Following these observations, we determined the hole distribution in the valence band (HOMO) and electron distribution of the conduction band (LUMO) of these materials, as shown in Figure 1e. While the HOMO of undoped g-C<sub>3</sub>N<sub>4</sub> is relatively delocalized, the LUMO exhibits a staggered distribution on alternating trimers. The same trend is observed for the LUMO of carbon-doped systems, though  $N_2 \rightarrow C$  doped g-C<sub>3</sub>N<sub>4</sub> exhibits a higher degree of localization due to a pronounced "tenting" of the g-C<sub>3</sub>N<sub>4</sub> sheet. The HOMO of carbon-doped g-C<sub>3</sub>N<sub>4</sub> is markedly different from the undoped material and is distributed around the dopant site. While the orbital structure will undergo remodeling subsequent to exciton formation and charge migration, it is reasonable to speculate that the impuritylocalized valence electrons provide the primary sites for localized hole formation within the valence band of doped g-C<sub>3</sub>N<sub>4</sub>. Prior theoretical investigations have indicated that charge migration between adjacent tri-s-triazine units is unlikely, underscoring this supposition.<sup>60</sup> In any event, our results indicate that DFT calculations can provide fundamental insights into the mechanism by which doping can improve redox and reactivity characteristics of g-C<sub>3</sub>N<sub>4</sub>.

The effect of nonmetal doping on the photocatalytic performance of g-C<sub>3</sub>N<sub>4</sub> was evaluated by testing MCB<sub>x</sub> or MCE, for phenol and/or atrazine degradation under simulated visible sunlight irradiation ( $\lambda > 400$  nm, xenon lamp) and comparing the activity with MC. As shown in Figure S3, the synthesized MCB<sub>x</sub> exhibited significantly enhanced photocatalytic activity, especially at the low barbituric acid content (i.e., x = 0.01-0.07). MCB<sub>0.07</sub> had the highest reaction rate constant, and its reactivity was enhanced by 2.8-fold compared to that of MC (0.8  $\pm$  0.08 vs 0.3  $\pm$  0.02 m<sup>2</sup> (mol of photons)<sup>-1</sup>). The photocatalytic activity of MCB<sub>x</sub> significantly decreased at higher barbituric acid mass loadings (x > 0.1), likely due to excessive carbon doping promoting charge recombination. 48 An optimum dopant level is necessary to improve charge separation and photocatalytic activity. However, phosphorus doping did not enhance the photocatalytic activity for phenol degradation at any dopant loading (i.e., y =0.01-0.5), though phosphorus uniformly doped into the g-C<sub>3</sub>N<sub>4</sub> structure (Figure S4). Reactivity increase was observed for atrazine degradation only on MCE<sub>0.01</sub> that had the lowest phosphorus doping level (0.6  $\pm$  0.1 and 0.3  $\pm$  0.02 m<sup>2</sup> (mol of photons)<sup>-1</sup> for MCE<sub>0.01</sub> and MC, respectively), as shown in Figure S5. The experimental results are in agreement with DFT simulation results with carbon-doped g-C<sub>3</sub>N<sub>4</sub> showing an enhanced activity compared to that of phosphorus-doped g-C<sub>3</sub>N<sub>4</sub>. The carbon-doped supramolecule-based g-C<sub>3</sub>N<sub>4</sub> with an optimum photocatalytic activity (MCB<sub>0.07</sub>), undoped supramolecule-based g-C<sub>3</sub>N<sub>4</sub> (MC), and conventional g-C<sub>3</sub>N<sub>4</sub> (U and M) were selected for further material characterization and water treatment applications.

Characterization of g-C<sub>3</sub>N<sub>4</sub>. Previous studies have confirmed that melamine and cyanuric acid formed a supramolecular complex for g-C<sub>3</sub>N<sub>4</sub> synthesis by XRD and FTIR. 34,35,38 All g-C<sub>3</sub>N<sub>4</sub> samples had a similar XRD pattern that could be ascribed to a typical graphite-like structure (Figure S6), and the introduction of cyanuric acid and/or barbituric acid may promote polymer-like growth and more defects in g- $C_3N_4$ .  $^{44,48,74}$  Infrared spectroscopic analysis of each photocatalyst (Figure S7) showed absorption bands characteristic of g-C<sub>3</sub>N<sub>4</sub>: six bands in the 1200–1650 cm<sup>-1</sup> region for stretching modes of C-N heterocycles<sup>75</sup> and one band at 805 cm<sup>-1</sup> for triazine. 76 The characteristic binding energy of g-C<sub>3</sub>N<sub>4</sub> was also observed in XPS spectra of each photocatalyst (Figure S8). <sup>28,77–79</sup> The results are very consistent with the previous reports, <sup>28,75–80</sup> confirming the presence of g-C<sub>3</sub>N<sub>4</sub>.

The morphology of g-C<sub>3</sub>N<sub>4</sub> was characterized by SEM and TEM, as shown in Figure 2a. U exhibited a porous structure, possibly due to a large amount of gas production in the thermal polycondensation of urea (e.g., NH<sub>3</sub> and H<sub>2</sub>O).<sup>81</sup> A typical condensed, layered structure of M was observed with the presence of fewer pores, likely due to a lesser extent of structural reorganization and reduced gas emission. 24,82 The addition of cyanuric acid created a loose, porous structure in MC, as expected from the self-templating of cyanuric acid with limited thermal stability.<sup>44</sup> Further introduction of barbituric acid for MCB<sub>0.07</sub> synthesis did not lead to any notable change in the sample morphology, possibly because of the low loading of barbituric acid (i.e., 0.07 g). The morphology of supramoleculebased g-C<sub>3</sub>N<sub>4</sub> is largely determined by the surface energy of the hydrogen-bonded supramolecular complex in a solvent. 34,35,3 A pancake-like structure and an irregular rod-/particle-like structure were observed for the supramolecular complex in ethanol and water, respectively (Figure S9). Accordingly, our samples showed a distinct porous structure compared to that reported by Shalom et al.<sup>35</sup> because ethanol rather than water was used in our work.

The surface area and porosity of g-C<sub>3</sub>N<sub>4</sub> samples were characterized by liquid N2 adsorption (Figure 2a), and the adsorption isotherms and pore size distribution (Figure S10) indicated that U, MC, and  $MCB_{0.07}$  mainly contained mesopores. M had the lowest BET surface area and pore volume in all g-C<sub>3</sub>N<sub>4</sub> samples, as supported by the SEM and TEM results. The BET surface area and pore volume of MC increased by 8.0- and 6.6-fold compared to those of M and were also higher than those of U. MCB<sub>0.07</sub> had the highest surface area and pore volume compared to other g-C<sub>3</sub>N<sub>4</sub>

Bulk carbon and nitrogen contents of g-C<sub>3</sub>N<sub>4</sub> were also analyzed (Figure 2a), and U and M had the same carbon to nitrogen (C/N) mass ratio of 0.59. The addition of cyanuric acid for MC synthesis increased C/N mass ratio to 0.60, and the addition of barbituric acid for MCB<sub>0.07</sub> synthesis further increased the C/N mass ratio to 0.61.

Optical properties of g-C<sub>3</sub>N<sub>4</sub>, including band gap and optical absorption, were characterized to evaluate its capability of harvesting and utilizing visible photons. g-C<sub>3</sub>N<sub>4</sub> is an indirect band gap photocatalyst, 83 and all g-C<sub>3</sub>N<sub>4</sub> samples had a similar band gap of 2.72 eV (harvesting photons with  $\lambda \le ca$ . 460 nm, Figure S11), which is in agreement with previous research and our DFT simulation results for undoped  $g\text{-}C_3N_4$ .  $^{24,26,81}$  The addition of cyanuric acid and barbituric acid did not change the band gap of g-C<sub>3</sub>N<sub>4</sub>, in contrast to DFT predictions, likely due to the low dopant level (C/N mass ratio of 0.61 vs 0.59). Nevertheless, MCB<sub>0.07</sub> showed noticeable band-tail absorption in the visible light region (>460 nm) compared to undoped g-C<sub>3</sub>N<sub>4</sub> (U, M, and MC in Figure S11), likely due to the presence of midgap states, i.e., the electronic states located within the band gap. The midgap states can accommodate photoexcited electrons from the valence band, resulting in the absorption of photons with energies smaller than the band gap for photocatalytic reactions. 51,84,85 In addition to intrinsic photon absorption as reflected by the band gap, the morphology, structure, and particle size of g-C<sub>3</sub>N<sub>4</sub> in reaction suspension may also impact the photon absorption due to light reflection and scattering on materials. 48 U had the highest absorption of visible light ( $\lambda > 400$  nm), followed by the other samples (i.e., M, MC, and MCB<sub>0.07</sub>) with similar optical absorption, as shown in Figure S12. Increased photon absorption of U may improve the photocatalytic activity for contaminant degradation.

Improved charge separation may enhance the photocatalytic activity of g-C<sub>3</sub>N<sub>4</sub> because of an increased amount of charge carriers for photocatalytic reactions. PL intensity, representative of radiative charge recombination, was used as an indirect evidence to characterize charge separation. The PL intensity of U, MC, and MCB<sub>0.07</sub> was similar and significantly lower than that of M (Figure S13), and it suggests that charge recombination may be the most pronounced in M, and its photocatalytic performance may be limited. The PL peak of U, MC, and MCB<sub>0.07</sub> also red-shifted compared to that of M (Figure S13). The reduction of PL intensity and red-shifted peaks indicate that the addition of cyanuric acid and barbituric acid for the preparation of supramolecule-based g-C<sub>3</sub>N<sub>4</sub> may lower the charge recombination compared to M derived from melamine only. Holes are generally less mobile than electrons (i.e., diffusion length of several nanometers vs micrometers), 86 and increased surface area and porosity in U, MC, and MCB<sub>0.07</sub> could facilitate the migration of holes to the surface and subsequent reactions with contaminants rather than recombination with electrons. 43 Carbon dopants may also facilitate hole localization and improve the reaction between charge carriers and contaminants, as suggested by DFT simulations. Nevertheless, the PL only qualitatively characterizes the extent of radiative charge recombination but not nonradiative charge recombination (dissipation as heat rather than photon emission), and it may not necessarily explain the photocatalytic activity. For example, the PL intensity of U and MC was lower compared to that of MCB<sub>0.07</sub>, which suggested that U and MC might exhibit an increased charge separation. In contrast, the photocatalytic activity of MCB<sub>0.07</sub> was equal to or higher than that of U and MC for contaminant degradation (Figure 2b). More quantitative analyses such as time-resolved fluorescence measurements 43,44 and theoretical simulations for charge

lifetime<sup>87,88</sup> are needed to correlate photocatalytic activity with the charge separation.

Relationship between Photocatalytic Activity and g-C<sub>3</sub>N<sub>4</sub> Properties. Figure 2b shows photocatalytic degradation kinetics of phenol and persistent organic micropollutants on g-C<sub>3</sub>N<sub>4</sub> in the phosphate buffer under simulated visible sunlight irradiation ( $\lambda > 400$  nm, xenon lamp). MCB<sub>0.07</sub> showed the highest photocatalytic activity for atrazine, sulfamethoxazole, and carbamazepine compared to that of other g-C<sub>3</sub>N<sub>4</sub> samples, and its reactivity was on par with U for phenol degradation. M had the lowest reactivity compared to that of its counterpart g-C<sub>3</sub>N<sub>4</sub> samples. Of the four probe contaminants, atrazine is the most photocatalytically degradable on g-C<sub>3</sub>N<sub>4</sub> samples (except for U), and carbamazepine is the most persistent in photocatalytic reactions. Atrazine degradation was also explored on MCB<sub>0.07</sub> over four repeated cycles, and no reactivity loss or morphological/chemical property change of the photocatalyst was observed (Figure S14).

The measured photocatalytic activity for contaminant degradation could be influenced by mass transfer and contaminant adsorption on g-C<sub>3</sub>N<sub>4</sub>. Nonetheless, mass transfer limitation was eliminated in the reaction (see the Supporting Information), and no contaminant adsorption was measured in the dark experiments. In addition, all g-C<sub>3</sub>N<sub>4</sub> samples in our study showed a similar negative  $\zeta$ -potential (i.e., -28.5 to -37.8 mV at pH 7.3), and they were not expected to interact strongly with neutral contaminants in the reaction solution at pH 7.3 (p $K_a$ 's of phenol, atrazine, sulfamethoxazole, and carbamazepine are 10.0, 1.7, 1.4/5.8, 2.3/13.9, respectively). <sup>89–92</sup>

The enhancement of photocatalytic activity could be determined by the following key photocatalyst properties: (i) an increased surface area, (ii) improved light harvesting, and (iii) promoted charge separation. Photocatalysis is a surfacemediated reaction, and the increased surface area provides more active sites for the contaminants to reside and react. The improvement of light harvesting and charge separation enables the generation of more electrons and holes for photocatalytic reactions. MCB<sub>0.07</sub> exhibited the highest surface area, and its reactivity outperformed M and MC for the degradation of all probe contaminants. The charge separation of MCB<sub>0.07</sub> and MC was significantly promoted compared to M, and M showed the lowest reactivity for contaminant degradation. The low carbon doping of MCB<sub>0.07</sub> did not change its band gap, but midgap states possibly increased visible light absorption and photocatalytic activity. The results indicate that the enhanced surface area, visible light absorption, and charge separation of MCB<sub>0.07</sub> synergistically contribute to improving the photocatalytic activity. 26,44,48

Selective Contaminant Degradation on g-C<sub>3</sub>N<sub>4</sub>. It is worth noting that g-C<sub>3</sub>N<sub>4</sub> is selective for contaminant degradation, e.g., MCB<sub>0.07</sub> is 1.8 times more reactive for the degradation of atrazine than phenol; however, U is 3.9 times more reactive for the degradation of phenol than atrazine. Similar selective degradation of sulfamethoxazole was also observed in comparison with phenol or atrazine. To understand the mechanism of selective contaminant removal, we explored the significance of the ROS and hole for the photocatalytic degradation of phenol and atrazine. Scavenger tests were conducted to quench the reactions between contaminants and a specific oxidative species, and the inhibition of reactivity was used to evaluate the contribution of the specific oxidative species to photocatalytic degradation. The results, as shown in

Figure S15a, indicated that the addition of *tert*-butyl alcohol, a · OH scavenger, reduced the reactivity for phenol degradation by 60% on U compared to 33% on MCB $_{0.07}$ . The ·OH scavenger test also showed 55% of reactivity inhibition for atrazine degradation on U, in contrast to no inhibition for atrazine degradation on MCB $_{0.07}$ . However, the addition of ammonium oxalate, a hole scavenger, significantly inhibited the reactivity for phenol and atrazine degradation on both U and MCB $_{0.07}$  from 74 to 86%. The addition of L-histidine, a  $^1\text{O}_2$  scavenger, reduced the reactivity of phenol degradation by 76% on U compared to 55% on MCB $_{0.07}$  and fully inhibited the reactivity for atrazine degradation on both U and MCB $_{0.07}$ .

We propose that the production of oxidative species on g-C<sub>3</sub>N<sub>4</sub> is structurally sensitive, i.e., different g-C<sub>3</sub>N<sub>4</sub> generates different types and amounts of oxidative species. Phenol is known to be more reactive with ·OH than atrazine with ·OH, and the second-order rate constant of ·OH-phenol is 5.9-fold higher than that of ·OH-atrazine  $(1.4 \times 10^{10} \text{ vs } 2.4 \times 10^9 \text{ s}^{-1})$ M-1).93,94 U may generate more ·OH than MCB<sub>0.07</sub>, and quenching ·OH had more pronounced inhibition for phenol degradation. MCB<sub>0.07</sub> may produce a significant amount of other ROS, e.g.,  $O_2^-\cdot/HO_2\cdot$  and  $^1O_2$ , to facilitate atrazine degradation. Though ·OH is generally more reactive (secondorder reaction rate constant between ROS and organics are  $10^6-10^{10}$ ,  $10^3-10^{10}$ , or  $<10^8~M^{-1}~s^{-1}$  for ·OH,  $^1O_2$ , or  $O_2^{-\cdot}/HO_2$ , respectively),  $^{95-97}$  its steady-state concentration is orders of magnitude lower in water compared to that of other ROS.  $^{98,99}$  The other ROS, especially  $^{1}O_{2}$ , may be a leading contributor to atrazine degradation; quenching ·OH had a negligible effect on atrazine degradation on MCB<sub>0.07</sub>, but quenching <sup>1</sup>O<sub>2</sub> completely deactivated photocatalytic atrazine degradation. In contrast, U could produce ·OH as one dominant ROS, and hence atrazine degradation on U is slower, and quenching ·OH reduces the reactivity significantly. The hole and <sup>1</sup>O<sub>2</sub> are the most dominant oxidative species for contaminant degradation, regardless of g-C<sub>3</sub>N<sub>4</sub> properties. O<sub>2</sub><sup>-</sup>· and H<sub>2</sub>O<sub>2</sub> were also identified in the photocatalytic degradation of phenol on U, and their contribution to reaction kinetics was also critical (Figure S15b). A recent study also demonstrated that the production of oxidative species is structurally sensitive, with g-C<sub>3</sub>N<sub>4</sub> nanosheets producing more H<sub>2</sub>O<sub>2</sub> than its bulk counterpart.

The exploration of the structural sensitivity is significant for the application of g-C<sub>3</sub>N<sub>4</sub> in contaminant degradation because we may tailor the synthesis and properties of g-C<sub>3</sub>N<sub>4</sub> to selectively degrade a certain group of highly toxic, low concentration contaminants with minimized inhibition from cocontaminants, natural water constituents, or foulants. It may also be useful for designing photocatalysts for selective oxidation and conversion of contaminants to value-added products (e.g., benzene oxidation to phenol). 100 Further study is required to quantitatively analyze the production of oxidative species and identify key g-C<sub>3</sub>N<sub>4</sub> properties for the selective generation of oxidative species and degradation of contaminants. Factors beyond the generation of oxidative species, such as the affinity of g-C<sub>3</sub>N<sub>4</sub> to contaminants, may also be important for the selectivity in contaminant degradation. The affinity between the photocatalyst and contaminant may be tailored for selective reactions.

Performance Comparison in Matrixes Representative of Water and Wastewater Treatment. For all experiments conducted in the simulated and real water samples and with both fresh and aged MCB<sub>0.07</sub>, little to no inhibition was

observed in atrazine degradation, as shown in Figure S16. The excellent photocatalytic performance of g-C<sub>3</sub>N<sub>4</sub> in complex water matrixes may be attributed to the large surface area, high porosity, the polymeric nature of the material without metal loading, and the selective ROS production.

Increased surface area and porosity may afford sufficient sites to interact with contaminants even when foulants or natural water constituents are at a high concentration (i.e., mM of foulants or constituents vs  $\mu M$  of contaminants). Noble metals used in photocatalysis (e.g., Au) are reactive and susceptible to and the polymeric nature of g-C<sub>3</sub>N<sub>4</sub> with the presence of only carbon and nitrogen mitigates the likelihood of photocatalyst deactivation. In addition, the hydrophilic nature of g-C<sub>3</sub>N<sub>4</sub> reduces the adsorption of organic or biological foulants, and the tri-s-triazine unit in g-C<sub>3</sub>N<sub>4</sub> is not expected to bind strongly to the carboxylate group of NOM, in contrast to TiO2.101

The selective production of ROS may also contribute to the minimal inhibition of photocatalytic activity in complex water matrixes. ·OH is the most powerful, nonselective radical generated in most AOPs and is attractive for environmental applications because it can degrade most organic contaminants at near diffusion-limited rates. 95,102,103 However, the nonselective destruction of contaminants can be easily compromised when nontarget chemicals are present, including NOM and other background constituents present in raw natural water or (partially) treated water and wastewater. 104,105 In our system,  $MCB_{0.07}$  may generate other ROS predominantly rather than OH, such as  ${}^{1}O_{2}$  and  ${}^{0}O_{2}$ -/H $O_{2}$ -, which are more selective for contaminant degradation. For example, <sup>1</sup>O<sub>2</sub> selectively oxidizes electron-rich moieties of contaminants with the presence of NOM,  $^{99,106}$  and  $O_2$ -·/HO $_2$ · facilitates the degradation of halogenated compounds because of the synergy of reductive dehalogenation and the oxidation of carbon backbones (O2-·/HO2· can act as both a reductant and an oxidant).1

Environmental Implication. Our study indicates that g-C<sub>3</sub>N<sub>4</sub> is a promising visible-light-responsive photocatalyst for water treatment applications because it is prepared from earth abundant materials, it exhibits highly tunable properties, and it shows excellent performance for the removal of persistent organic micropollutants in complex water matrixes. N-rich organic wastes (e.g., urea) could be reused to synthesize g-C<sub>3</sub>N<sub>4</sub>, improving the sustainability of material production. We rationally designed supramolecule-based g-C<sub>3</sub>N<sub>4</sub> with enhanced surface area and charge separation by soft-templating and nonmetal doping, and the material with improved photocatalytic performance, economic feasibility, sustainability, and robustness was obtained. DFT simulations were used to understand the mechanism of nonmetal doping for g-C<sub>3</sub>N<sub>4</sub> that was largely unknown in previous studies, and simulation results successfully predicted the photocatalytic performance for contaminant degradation. Our study provides first insights into the rational material design guided by DFT simulations, which is highly needed for material-based research for environmental applications.

Selective contaminant degradation was observed on g-C<sub>3</sub>N<sub>4</sub> with distinct properties, likely due to the difference in ROS production and interfacial interactions between the contaminant and the photocatalyst. The selectivity of g-C<sub>3</sub>N<sub>4</sub> paves a new avenue for the smart design of photocatalysts for a wide range of applications. 100,108 Little to no inhibition of the photocatalytic activity in complex water matrixes implies that gC<sub>3</sub>N<sub>4</sub> is robust for water purification in the presence of natural water constituents and foulants. g-C<sub>3</sub>N<sub>4</sub> is a versatile visiblelight-responsive photocatalyst and holds promise for a range of environmental applications, including the development of point-of-use or point-of-entry water treatment units for small public water systems that are more susceptible to contamination 109,110 and use as an antimicrobial material to prevent pathogen transmission and disease outbreaks. 32,33

Before g-C<sub>3</sub>N<sub>4</sub> may be practically deployed, it is critical to understand the mechanism of ROS production and interfacial interactions between the contaminant and the photocatalyst. Photocatalyst stability for a long-term reaction should be evaluated by considering photocatalyst self-corrosion and deactivation with the presence of foulants. Immobilization of g-C<sub>3</sub>N<sub>4</sub>, combination of g-C<sub>3</sub>N<sub>4</sub> with other photocatalysts, and optimized reactor design will minimize photocatalyst postseparation, reduce photocatalyst leaching, maximize solar energy harvesting, enhance mass transfer, and improve photon efficiency for reactions.

#### ASSOCIATED CONTENT

# S Supporting Information

The Supporting Information is available free of charge on the ACS Publications Website at DOI: 10.1021/acs.est.6b02579.

Experimental and simulation details; spectral irradiance, photon fluence, and optical power density of the light source; description of water treatment process in GWP, wastewater treatment process in BRWRF, and water quality parameters; band gap, CBM, and VBM of g-C<sub>3</sub>N<sub>4</sub>; mass transfer evaluation; material characterization results; photocatalytic activity of g-C<sub>3</sub>N<sub>4</sub> in a model buffer system with the presence of scavengers and in simulated/real complex water matrixes (PDF)

#### AUTHOR INFORMATION

# **Corresponding Author**

\*Phone: 202-994-0506; fax: 202-994-0127; e-mail: danmengshuai@gwu.edu; website: http://materwatersus. weebly.com/.

#### ORCID ®

Wen Zhang: 0000-0001-8413-0598

The authors declare no competing financial interest.

# ACKNOWLEDGMENTS

We acknowledge the NSF Grant CBET-1437989, GW CEE and Chemistry Department start-up grants, GW Columbian College Facilitating Fund, and JHU Water SEED grant for supporting our study. Computational resources were provided under DOE contract DE-AC02-06CH11357 and NSF contract TG-CHE130008. We thank USNA, Elizabeth Eves and Dr. Julio A. N. T. Soares at UIUC, and Dr. Michael Jean-Claude Nalbandian at UCR for the support in materials characterization. We also thank John J. Hanchak at GWP and Michael R. Rumke at BRWRF for providing water samples.

### REFERENCES

(1) Occurrence of contaminants of emerging concern in wastewater from nine publicly owned treatment works. EPA 821-R-09-009; Office of Water, U.S. Environmental Protection Agency: Washington, DC,

- (2) Treating contaminants of emerging concern: A literature review database. EPA-820-R-10-002; Office of Water, U.S. Environmental Protection Agency: Washington, DC, 2010.
- (3) Oulton, R. L.; Kohn, T.; Cwiertny, D. M. Pharmaceuticals and personal care products in effluent matrixes: A survey of transformation and removal during wastewater treatment and implications for wastewater management. J. Environ. Monit. 2010, 12 (11), 1956-1978.
- (4) Pharmaceuticals in drinking-water. World Health Organization: Geneva, Switzerland, 2012.
- (5) Homem, V.; Santos, L. Degradation and removal methods of antibiotics from aqueous matrixes - A review. J. Environ. Manage. 2011, 92 (10), 2304-2347.
- (6) Prieto-Rodríguez, L.; Oller, I.; Klamerth, N.; Agüera, A.; Rodríguez, E. M.; Malato, S. Application of solar AOPs and ozonation for elimination of micropollutants in municipal wastewater treatment plant effluents. Water Res. 2013, 47 (4), 1521-1528.
- (7) Hoffmann, M. R.; Martin, S. T.; Choi, W. Y.; Bahnemann, D. W. Environmental applications of semiconductor photocatalysis. Chem. Rev. 1995, 95 (1), 69-96.
- (8) Pelaez, M.; Nolan, N. T.; Pillai, S. C.; Seery, M. K.; Falaras, P.; Kontos, A. G.; Dunlop, P. S. M.; Hamilton, J. W. J.; Byrne, J. A.; O'Shea, K.; Entezari, M. H.; Dionysiou, D. D. A review on the visible light active titanium dioxide photocatalysts for environmental applications. Appl. Catal., B 2012, 125, 331-349.
- (9) Kim, J.; Lee, C. W.; Choi, W. Platinized WO<sub>3</sub> as an environmental photocatalyst that generates OH radicals under visible light. Environ. Sci. Technol. 2010, 44 (17), 6849-6854.
- (10) Huang, G.; Ma, Z.; Huang, W.; Tian, Y.; Jiao, C.; Yang, Z.; Wan, Z.; Pan, A. Ag<sub>3</sub>PO<sub>4</sub> semiconductor photocatalyst: Possibilities and challenges. J. Nanomater. 2013, 2013, 1-8.
- (11) Huang, Z.; Pan, L.; Zou, J.; Zhang, X.; Wang, L. Nanostructured bismuth vanadate-based materials for solar-energy-driven water oxidation: A review on recent progress. Nanoscale 2014, 6 (23), 14044-14063
- (12) Ye, L.; Su, Y.; Jin, X.; Xie, H.; Zhang, C. Recent advances in BiOX (X = Cl, Br and I) photocatalysts: Synthesis, modification, facet effects and mechanisms. Environ. Sci.: Nano 2014, 1 (2), 90-112.
- (13) Zyoud, A. H.; Zaatar, N.; Saadeddin, I.; Ali, C.; Park, D.; Campet, G.; Hilal, H. S. CdS-sensitized TiO2 in phenazopyridine photo-degradation: Catalyst efficiency, stability and feasibility assessment. J. Hazard. Mater. 2010, 173 (1-3), 318-325.
- (14) Lo, S. C.; Lin, C. F.; Wu, C. H.; Hsieh, P. H. Capability of coupled CdSe/TiO<sub>2</sub> for photocatalytic degradation of 4-chlorophenol. J. Hazard. Mater. 2004, 114 (1-3), 183-190.
- (15) Cates, E. L.; Chinnapongse, S. L.; Kim, J.; Kim, J. Engineering light: Advances in wavelength conversion materials for energy and environmental technologies. Environ. Sci. Technol. 2012, 46 (22), 12316-12328.
- (16) Hu, Y.; Gao, X.; Yu, L.; Wang, Y.; Ning, J.; Xu, S.; Lou, X. W. Carbon-coated CdS petalous nanostructures with enhanced photostability and photocatalytic activity. Angew. Chem., Int. Ed. 2013, 52 (21), 5636-5639.
- (17) Cui, Y.; Ding, Z.; Fu, X.; Wang, X. Construction of conjugated carbon nitride nanoarchitectures in solution at low temperatures for photoredox catalysis. Angew. Chem., Int. Ed. 2012, 51 (47), 11814-
- (18) Maeda, K.; Wang, X.; Nishihara, Y.; Lu, D.; Antonietti, M.; Domen, K. Photocatalytic activities of graphitic carbon nitride powder for water reduction and oxidation under visible light. J. Phys. Chem. C 2009, 113 (12), 4940-4947.
- (19) National Renewable Energy Laboratory. Reference solar spectral irradiance: Air mass 1.5. http://rredc.nrel.gov/solar/spectra/am1.5/ (accessed April 4, 2016).
- (20) Cao, S.; Low, J.; Yu, J.; Jaroniec, M. Polymeric photocatalysts based on graphitic carbon nitride. Adv. Mater. 2015, 27 (13), 2150-2176.
- (21) Zhang, J.; Grzelczak, M.; Hou, Y.; Maeda, K.; Domen, K.; Fu, X.; Antonietti, M.; Wang, X. Photocatalytic oxidation of water by

- polymeric carbon nitride nanohybrids made of sustainable elements. Chem. Sci. 2012, 3 (2), 443-446.
- (22) Sano, T.; Tsutsui, S.; Koike, K.; Hirakawa, T.; Teramoto, Y.; Negishi, N.; Takeuchi, K. Activation of graphitic carbon nitride (g-C<sub>3</sub>N<sub>4</sub>) by alkaline hydrothermal treatment for photocatalytic NO oxidation in gas phase. J. Mater. Chem. A 2013, 1 (21), 6489-6496.
- (23) Ayan-Varela, M.; Villar-Rodil, S.; Paredes, J. I.; Munuera, J. M.; Pagan, A.; Lozano-Perez, A. A.; Cenis, J. L.; Martinez-Alonso, A.; Tascon, J. M. D. Investigating the dispersion behavior in solvents, biocompatibility, and use as support for highly efficient metal catalysts of exfoliated graphitic carbon nitride. ACS Appl. Mater. Interfaces 2015, 7 (43), 24032–24045.
- (24) Yan, S. C.; Li, Z. S.; Zou, Z. G. Photodegradation performance of g-C<sub>3</sub>N<sub>4</sub> fabricated by directly heating melamine. Langmuir 2009, 25 (17), 10397-10401.
- (25) Chu, S.; Wang, Y.; Guo, Y.; Feng, J.; Wang, C.; Luo, W.; Fan, X.; Zou, Z. Band structure engineering of carbon nitride: In search of a polymer photocatalyst with high photooxidation property. ACS Catal. **2013**, 3 (5), 912–919.
- (26) Jun, Y.; Lee, E. Z.; Wang, X.; Hong, W. H.; Stucky, G. D.; Thomas, A. From melamine-cyanuric acid supramolecular aggregates to carbon nitride hollow spheres. Adv. Funct. Mater. 2013, 23 (29),
- (27) Kumar, S.; Baruah, A.; Tonda, S.; Kumar, B.; Shanker, V.; Sreedhar, B. Cost-effective and eco-friendly synthesis of novel and stable N-doped ZnO/g- $C_3N_4$  core-shell nanoplates with excellent visible-light responsive photocatalysis. Nanoscale 2014, 6 (9), 4830-
- (28) Liu, J.; Zhang, T.; Wang, Z.; Dawson, G.; Chen, W. Simple pyrolysis of urea into graphitic carbon nitride with recyclable adsorption and photocatalytic activity. J. Mater. Chem. 2011, 21 (38), 14398-14401.
- (29) Xu, H.; Yan, J.; She, X.; Xu, L.; Xia, J.; Xu, Y.; Song, Y.; Huang, L.; Li, H. Graphene-analogue carbon nitride: Novel exfoliation synthesis and its application in photocatalysis and photoelectrochemical selective detection of trace amount of Cu<sup>2+</sup>. Nanoscale 2014, 6 (3), 1406-1415.
- (30) Wang, Y.; Shi, R.; Lin, J.; Zhu, Y. Enhancement of photocurrent and photocatalytic activity of ZnO hybridized with graphite-like C<sub>3</sub>N<sub>4</sub>. Energy Environ. Sci. 2011, 4 (8), 2922-2929.
- (31) Huang, J.; Ho, W.; Wang, X. Metal-free disinfection effects induced by graphitic carbon nitride polymers under visible light illumination. Chem. Commun. 2014, 50 (33), 4338-4340.
- (32) Zhao, H.; Yu, H.; Quan, X.; Chen, S.; Zhang, Y.; Zhao, H.; Wang, H. Fabrication of atomic single layer graphitic-C<sub>3</sub>N<sub>4</sub> and its high performance of photocatalytic disinfection under visible light irradiation. Appl. Catal., B 2014, 152, 46-50.
- (33) Wang, W.; Yu, J. C.; Xia, D.; Wong, P. K.; Li, Y. Graphene and g-C<sub>3</sub>N<sub>4</sub> nanosheets cowrapped elemental alpha-sulfur as a novel metalfree heterojunction photocatalyst for bacterial inactivation under visible-light. Environ. Sci. Technol. 2013, 47 (15), 8724-8732.
- (34) Shalom, M.; Inal, S.; Fettkenhauer, C.; Neher, D.; Antonietti, M. Improving carbon nitride photocatalysis by supramolecular preorganization of monomers. J. Am. Chem. Soc. 2013, 135 (19), 7118-7121.
- (35) Shalom, M.; Guttentag, M.; Fettkenhauer, C.; Inal, S.; Neher, D.; Llobet, A.; Antonietti, M. In situ formation of heterojunctions in modified graphitic carbon nitride: Synthesis and noble metal free photocatalysis. Chem. Mater. 2014, 26 (19), 5812-5818.
- (36) Jun, Y.; Park, J.; Lee, S. U.; Thomas, A.; Hong, W. H.; Stucky, G. D. Three-dimensional macroscopic assemblies of low-dimensional carbon nitrides for enhanced hydrogen evolution. Angew. Chem. 2013, 125 (42), 11289-11293.
- (37) Ishida, Y.; Chabanne, L.; Antonietti, M.; Shalom, M. Morphology control and photocatalysis enhancement by the one-pot synthesis of carbon nitride from preorganized hydrogen-bonded supramolecular precursors. Langmuir 2014, 30 (2), 447–451.
- (38) Liao, Y.; Zhu, S.; Ma, J.; Sun, Z.; Yin, C.; Zhu, C.; Lou, X.; Zhang, D. Tailoring the morphology of g-C<sub>3</sub>N<sub>4</sub> by self-assembly

- towards high photocatalytic performance. ChemCatChem 2014, 6 (12), 3419–3425.
- (39) Jordan, T.; Fechler, N.; Xu, J.; Brenner, T. J.; Antonietti, M.; Shalom, M. Caffeine doping" of carbon/nitrogen-based organic catalysts: Caffeine as a supramolecular edge modifier for the synthesis of photoactive carbon nitride tubes. *ChemCatChem* **2015**, 7 (18), 2826–2830.
- (40) Fukasawa, Y.; Takanabe, K.; Shimojima, A.; Antonietti, M.; Domen, K.; Okubo, T. Synthesis of ordered porous graphitic- $C_3N_4$  and regularly arranged  $Ta_3N_5$  nanoparticles by using self-assembled silica nanospheres as a primary template. *Chem. Asian J.* **2011**, *6* (1), 103–109.
- (41) Goettmann, F.; Fischer, A.; Antonietti, M.; Thomas, A. Chemical synthesis of mesoporous carbon nitrides using hard templates and their use as a metal-free catalyst for Friedel-Crafts reaction of benzene. *Angew. Chem., Int. Ed.* **2006**, 45 (27), 4467–4471.
- (42) Ong, W.; Tan, L.; Ng, Y. H.; Yong, S.; Chai, S. Graphitic carbon nitride (g-C<sub>3</sub>N<sub>4</sub>)-based photocatalysts for artificial photosynthesis and environmental remediation: Are we a step closer to achieving sustainability? *Chem. Rev.* **2016**, *116* (12), 7159–7329.
- (43) Niu, P.; Zhang, L.; Liu, G.; Cheng, H. Graphene-like carbon nitride nanosheets for improved photocatalytic activities. *Adv. Funct. Mater.* **2012**, 22 (22), 4763–4770.
- (44) Shalom, M.; Inal, S.; Fettkenhauer, C.; Neher, D.; Antonietti, M. Improving carbon nitride photocatalysis by supramolecular preorganization of monomers. *J. Am. Chem. Soc.* **2013**, *135* (19), 7118–7121.
- (45) Wang, X.; Chen, X.; Thomas, A.; Fu, X.; Antonietti, M. Metal-containing carbon nitride compounds: A new functional organic-metal hybrid material. *Adv. Mater.* **2009**, *21* (16), 1609–1612.
- (46) Yue, B.; Li, Q.; Iwai, H.; Kako, T.; Ye, J. Hydrogen production using zinc-doped carbon nitride catalyst irradiated with visible light. *Sci. Technol. Adv. Mater.* **2011**, *12* (3), 034401.
- (47) Zhang, G.; Lan, Z.; Lin, L.; Lin, S.; Wang, X. Overall water splitting by  $Pt/g-C_3N_4$  photocatalysts without using sacrificial agents. *Chem. Sci.* **2016**, 7 (5), 3062–3066.
- (48) Zhang, J.; Chen, X.; Takanabe, K.; Maeda, K.; Domen, K.; Epping, J. D.; Fu, X.; Antonietti, M.; Wang, X. Synthesis of a carbon nitride structure for visible-light catalysis by copolymerization. *Angew. Chem., Int. Ed.* **2010**, 49 (2), 441–444.
- (49) Zhang, Y.; Mori, T.; Ye, J. Polymeric carbon nitrides: Semiconducting properties and emerging applications in photocatalysis and photoelectrochemical energy conversion. *Sci. Adv. Mater.* **2012**, *4* (2), 282–291.
- (50) Zhou, Y.; Zhang, L.; Liu, J.; Fan, X.; Wang, B.; Wang, M.; Ren, W.; Wang, J.; Li, M.; Shi, J. Brand new P-doped  $g-C_3N_4$ : Enhanced photocatalytic activity for  $H_2$  evolution and rhodamine B degradation under visible light. *J. Mater. Chem. A* **2015**, 3 (7), 3862–3867.
- (51) Ran, J.; Ma, T. Y.; Gao, G.; Du, X.; Qiao, S. Z. Porous P-doped graphitic carbon nitride nanosheets for synergistically enhanced visible-light photocatalytic H<sub>2</sub> production. *Energy Environ. Sci.* **2015**, 8 (12), 3708–3717.
- (52) Zhang, Y.; Ligthart, D. A. J. M.; Quek, X.; Gao, L.; Hensen, E. J. M. Influence of Rh nanoparticle size and composition on the photocatalytic water splitting performance of Rh/graphitic carbon nitride. *Int. J. Hydrogen Energy* **2014**, *39* (22), 11537–11546.
- (53) Ma, S.; Zhan, S.; Jia, Y.; Shi, Q.; Zhou, Q. Enhanced disinfection application of ag-modified g-C<sub>3</sub>N<sub>4</sub> composite under visible light. *Appl. Catal., B* **2016**, *186*, 77–87.
- (54) Zheng, D.; Pang, C.; Wang, X. The function-led design of Z-scheme photocatalytic systems based on hollow carbon nitride semiconductors. *Chem. Commun.* **2015**, *51* (98), 17467–17470.
- (55) Nalbandian, M. J.; Greenstein, K. E.; Shuai, D.; Zhang, M.; Choa, Y.; Parkin, G. F.; Myung, N. V.; Cwiertny, D. M. Tailored synthesis of photoactive TiO<sub>2</sub> nanofibers and Au/TiO<sub>2</sub> nanofiber composites: Structure and reactivity optimization for water treatment applications. *Environ. Sci. Technol.* **2015**, *49* (3), 1654–1663.
- (56) Chaplin, B. P.; Shapley, J. R.; Werth, C. J. Regeneration of sulfur-fouled bimetallic Pd-based catalysts. *Environ. Sci. Technol.* **2007**, 41 (15), 5491–5497.

- (57) Guo, S.; Deng, Z.; Li, M.; Jiang, B.; Tian, C.; Pan, Q.; Fu, H. Phosphorus-doped carbon nitride tubes with a layered micronanostructure for enhanced visible-light photocatalytic hydrogen evolution. *Angew. Chem., Int. Ed.* **2016**, 55 (5), 1830–1834.
- (58) Zhu, Y.; Ren, T.; Yuan, Z. Y. Mesoporous phosphorus-doped g- $C_3N_4$  nanostructured flowers with superior photocatalytic hydrogen evolution performance. ACS Appl. Mater. Interfaces **2015**, 7 (30), 16850–16856.
- (59) Dong, G.; Zhao, K.; Zhang, L. Carbon self-doping induced high electronic conductivity and photoreactivity of g-C<sub>3</sub>N<sub>4</sub>. *Chem. Commun.* **2012**, 48 (49), 6178–6180.
- (60) Ma, X.; Lv, Y.; Xu, J.; Liu, Y.; Zhang, R.; Zhu, Y. A strategy of enhancing the photoactivity of g-C<sub>3</sub>N<sub>4</sub> via doping of nonmetal elements: A first-principles study. *J. Phys. Chem. C* **2012**, *116* (44), 23485–23493.
- (61) Hohenberg, P.; Kohn, W. Inhomogeneous electron gas. *Phys. Rev.* **1964**, *136*, B864–B871.
- (62) Kohn, W.; Sham, L. J. Self-consistent equations including exchange and correlation effects. *Phys. Rev.* **1965**, *140*, A1133–A1138.
- (63) Hutter, J.; Iannuzzi, M.; Schiffmann, F.; VandeVondele, J. CP2K: Atomistic simulations of condensed matter systems. *WIREs Comput. Mol. Sci.* **2014**, *4*, 15–25.
- (64) Zhang, Y.; Antonietti, M. Photocurrent generation by polymeric carbon nitride solids: An initial step towards a novel photovoltaic system. *Chem. Asian J.* **2010**, *5* (6), 1307–1311.
- (65) Deifallah, M.; McMillan, P. F.; Corà, F. Electronic and structural properties of two-dimensional carbon nitride graphenes. *J. Phys. Chem.* C **2008**, *112* (14), 5447–5453.
- (66) Wirth, J.; Neumann, R.; Antonietti, M.; Saalfrank, P. Adsorption and photocatalytic splitting of water on graphitic carbon nitride: A combined first principles and semiempirical study. *Phys. Chem. Chem. Phys.* **2014**, *16*, 15917–15926.
- (67) Zuluaga, S.; Liu, L.; Shafiq, N.; Rupich, S. M.; Veyan, J.; Chabal, Y. J.; Thonhauser, T. Structural band-gap tuning in g- $C_3N_4$ . *Phys. Chem. Chem. Phys.* **2015**, *17* (2), 957–962.
- (68) Melissen, S.; Bahers, T. L.; Steinmann, S. N.; Sautet, P. Relationship between carbon nitride structure and exciton binding energies: A DFT perspective. *J. Phys. Chem. C* **2015**, *119*, 25188–25196.
- (69) Nosaka, Y.; Takahashi, S.; Sakamoto, H.; Nosaka, A. Y. Reaction mechanism of Cu (II)-grafted visible-light responsive TiO<sub>2</sub> and WO<sub>3</sub> photocatalysts studied by means of ESR spectroscopy and chemiluminescence photometry. *J. Phys. Chem. C* **2011**, *115* (43), 21283–21290.
- (70) Teranishi, M.; Naya, S.; Tada, H. In situ liquid phase synthesis of hydrogen peroxide from molecular oxygen using gold nanoparticle-loaded titanium (IV) dioxide photocatalyst. *J. Am. Chem. Soc.* **2010**, 132 (23), 7850–7851.
- (71) Zhang, H.; Guo, L.; Zhao, L.; Wan, B.; Yang, Y. Switching oxygen reduction pathway by exfoliating graphitic carbon nitride for enhanced photocatalytic phenol degradation. *J. Phys. Chem. Lett.* **2015**, 6 (6), 958–963.
- (72) Shiraishi, Y.; Kanazawa, S.; Kofuji, Y.; Sakamoto, H.; Ichikawa, S.; Tanaka, S.; Hirai, T. Sunlight-driven hydrogen peroxide production from water and molecular oxygen by metal-free photocatalysts. *Angew. Chem.* **2014**, *126* (49), 13672–13677.
- (73) Zhang, Y.; Mori, T.; Ye, J.; Antonietti, M. Phosphorus-doped carbon nitride solid: Enhanced electrical conductivity and photocurrent generation. *J. Am. Chem. Soc.* **2010**, *132* (18), 6294–6295.
- (74) Dong, F.; Wu, L.; Sun, Y.; Fu, M.; Wu, Z.; Lee, S. C. Efficient synthesis of polymeric g- $C_3N_4$  layered materials as novel efficient visible light driven photocatalysts. *J. Mater. Chem.* **2011**, 21 (39), 15171–15174.
- (75) Li, X.; Zhang, J.; Shen, L.; Ma, Y.; Lei, W.; Cui, Q.; Zou, G. Preparation and characterization of graphitic carbon nitride through pyrolysis of melamine. *Appl. Phys. A: Mater. Sci. Process.* **2009**, *94* (2), 387–392.

- (76) Khabashesku, V. N.; Zimmerman, J. L.; Margrave, J. L. Powder synthesis and characterization of amorphous carbon nitride. *Chem. Mater.* **2000**, *12* (11), 3264–3270.
- (77) Kundu, S.; Xia, W.; Busser, W.; Becker, M.; Schmidt, D. A.; Havenith, M.; Muhler, M. The formation of nitrogen-containing functional groups on carbon nanotube surfaces: A quantitative XPS and TPD study. *Phys. Chem. Chem. Phys.* **2010**, *12* (17), 4351–4359.
- (78) Raymundo-Piñero, E.; Cazorla-Amorós, D.; Linares-Solano, A.; Find, J.; Wild, U.; Schlögl, R. Structural characterization of N-containing activated carbon fibers prepared from a low softening point petroleum pitch and a melamine resin. *Carbon* **2002**, *40* (4), 597–608.
- (79) Thomas, A.; Fischer, A.; Goettmann, F.; Antonietti, M.; Muller, J.; Schlogl, R.; Carlsson, J. M. Graphitic carbon nitride materials: Variation of structure and morphology and their use as metal-free catalysts. *J. Mater. Chem.* **2008**, *18* (41), 4893–4908.
- (80) Bojdys, M. J.; Mueller, J.; Antonietti, M.; Thomas, A. Ionothermal synthesis of crystalline, condensed, graphitic carbon nitride. *Chem. Eur. J.* **2008**, *14* (27), 8177–8182.
- (81) Zhang, Y.; Liu, J.; Wu, G.; Chen, W. Porous graphitic carbon nitride synthesized via direct polymerization of urea for efficient sunlight-driven photocatalytic hydrogen production. *Nanoscale* **2012**, *4* (17), 5300–5303.
- (82) Mao, J.; Peng, T.; Zhang, X.; Li, K.; Ye, L.; Zan, L. Effect of graphitic carbon nitride microstructures on the activity and selectivity of photocatalytic CO<sub>2</sub> reduction under visible light. *Catal. Sci. Technol.* **2013**, *3* (5), 1253–1260.
- (83) Wang, Y.; Di, Y.; Antonietti, M.; Li, H.; Chen, X.; Wang, X. Excellent visible-light photocatalysis of fluorinated polymeric carbon nitride solids. *Chem. Mater.* **2010**, 22 (18), 5119–5121.
- (84) Zhang, J.; Liu, S.; Yu, J.; Jaroniec, M. A simple cation exchange approach to Bi-doped ZnS hollow spheres with enhanced UV and visible-light photocatalytic H<sub>2</sub>-production activity. *J. Mater. Chem.* **2011**, 21 (38), 14655–14662.
- (85) Yaghoubi, H.; Li, Z.; Chen, Y.; Ngo, H. T.; Bhethanabotla, V. R.; Joseph, B.; Ma, S.; Schlaf, R.; Takshi, A. Toward a visible light-driven photocatalyst: The effect of midgap-states-induced energy gap of undoped TiO<sub>2</sub> nanoparticles. *ACS Catal.* **2015**, 5 (1), 327–335.
- (86) Fonash, S., Ed. Solar Cell Device Physics, 2nd ed.; Academic Press: 2010.
- (87) Mara, M. W.; Bowman, D. N.; Buyukcakir, O.; Shelby, M. L.; Haldrup, K.; Huang, J.; Harpham, M. R.; Stickrath, A. B.; Zhang, X.; Stoddart, J. F.; Coskun, A.; Jakubikova, E.; Chen, L. X. Electron injection from copper diimine sensitizers into TiO<sub>2</sub>: Structural effects and their implications for solar energy conversion devices. *J. Am. Chem. Soc.* **2015**, *137* (30), 9670–9684.
- (88) Li, J.; Li, H.; Winget, P.; Bredas, J. Electronic structure of the perylene-zinc oxide interface: Computational study of photoinduced electron transfer and impact of surface defects. *J. Phys. Chem. C* **2015**, 119 (33), 18843–18858.
- (89) Criquet, J.; Rodriguez, E. M.; Allard, S.; Wellauer, S.; Salhi, E.; Joll, C. A.; von Gunten, U. Reaction of bromine and chlorine with phenolic compounds and natural organic matter extracts electrophilic aromatic substitution and oxidation. *Water Res.* **2015**, *85*, 476–486.
- (90) Calisto, V.; Domingues, M. R. M.; Erny, G. L.; Esteves, V. I. Direct photodegradation of carbamazepine followed by micellar electrokinetic chromatography and mass spectrometry. *Water Res.* **2011**, *45* (3), 1095–1104.
- (91) Liu, P.; Zhang, H.; Feng, Y.; Shen, C.; Yang, F. Influence of spacer on rejection of trace antibiotics in wastewater during forward osmosis process. *Desalination* **2015**, *371*, 134–143.
- (92) Lekkerkerker-Teunissen, K.; Benotti, M. J.; Snyder, S. A.; van Dijk, H. C. Transformation of atrazine, carbamazepine, diclofenac and sulfamethoxazole by low and medium pressure UV and UV/H<sub>2</sub>O<sub>2</sub> treatment. *Sep. Purif. Technol.* **2012**, *96*, 33–43.
- (93) Huber, M. M.; Canonica, S.; Park, G. Y.; Von Gunten, U. Oxidation of pharmaceuticals during ozonation and advanced oxidation processes. *Environ. Sci. Technol.* **2003**, *37* (5), 1016–1024.
- (94) De, A. K.; Chaudhuri, B.; Bhattacharjee, S.; Dutta, B. K. Estimation of OH radical reaction rate constants for phenol and

- chlorinated phenols using  $UV/H_2O_2$  photo-oxidation. *J. Hazard. Mater.* **1999**, *64* (1), 91–104.
- (95) Antoniou, M. G.; Zhao, C.; O'Shea, K. E.; Zhang, G.; Dionysiou, D. D.; Zhao, C.; Han, C.; Nadagouda, M. N.; Choi, H.; Fotiou, T.; Triantis, T. M.; Hiskia, A. *Photocatalytic Degradation of Organic Contaminants in Water: Process Optimization and Degradation Pathways*; Royal Society of Chemistry: Croydon, CRO 4YY, U.K., 2016.
- (96) Wilkinson, F.; Helman, W. P.; Ross, A. B. Rate constants for the decay and reactions of the lowest electronically excited singlet state of molecular oxygen in solution. An expanded and revised compilation. *J. Phys. Chem. Ref. Data* **1995**, 24 (2), 663–677.
- (97) Bielski, B. H. J.; Cabelli, D. E.; Arudi, R. L.; Ross, A. B. Reactivity of  $HO_2/O_2^-$  radicals in aqueous solution. *J. Phys. Chem. Ref. Data* **1985**, *14* (4), 1041–1100.
- (98) Xia, D.; Shen, Z.; Huang, G.; Wang, W.; Yu, J. C.; Wong, P. K. Red phosphorus: An earth-abundant elemental photocatalyst for "green" bacterial inactivation under visible light. *Environ. Sci. Technol.* **2015**, *49* (10), *6264*–*6273*.
- (99) Brame, J.; Long, M.; Li, Q.; Alvarez, P. Trading oxidation power for efficiency: Differential inhibition of photo-generated hydroxyl radicals versus singlet oxygen. *Water Res.* **2014**, *60*, 259–266.
- (100) Chen, X.; Zhang, J.; Fu, X.; Antonietti, M.; Wang, X. Fe-g- $C_3N_4$ -catalyzed oxidation of benzene to phenol using hydrogen peroxide and visible light. *J. Am. Chem. Soc.* **2009**, *131* (33), 11658–11659.
- (101) Huang, X.; Leal, M.; Li, Q. Degradation of natural organic matter by  $TiO_2$  photocatalytic oxidation and its effect on fouling of low-pressure membranes. *Water Res.* **2008**, 42 (4–5), 1142–1150.
- (102) Neta, P.; Dorfman, L. M. Pulse radiolysis studies. XIII. Rate constants for the reaction of hydroxyl radicals with aromatic compounds in aqueous solutions. In *Radiation Chemistry*; American Chemical Society: 1968; Vol. 81, pp 222–230.
- (103) Haag, W. R.; Yao, C. C. D. Rate constants for reaction of hydroxyl radicals with several drinking-water contaminants. *Environ. Sci. Technol.* **1992**, *26* (5), 1005–1013.
- (104) Brame, J.; Long, M.; Li, Q.; Alvarez, P. Inhibitory effect of natural organic matter or other background constituents on photocatalytic advanced oxidation processes: Mechanistic model development and validation. *Water Res.* **2015**, *84*, 362–371.
- (105) Vongunten, U.; Hoigne, J. Bromate formation during ozonation of bromide-containing waters: Interaction of ozone and hydroxyl radical reactions. *Environ. Sci. Technol.* **1994**, 28 (7), 1234–1242.
- (106) Kim, H.; Kim, W.; Mackeyev, Y.; Lee, G.; Kim, H.; Tachikawa, T.; Hong, S.; Lee, S.; Kim, J.; Wilson, L. J.; Majima, T.; Alvarez, P. J. J.; Choi, W.; Lee, J. Selective oxidative degradation of organic pollutants by singlet oxygen-mediated photosensitization: Tin porphyrin versus  $C_{60}$  aminofullerene systems. *Environ. Sci. Technol.* **2012**, *46* (17), 9606–9613.
- (107) Hayyan, M.; Hashim, M. A.; AlNashef, I. M. Superoxide ion: Generation and chemical implications. *Chem. Rev.* **2016**, *116* (5), 3029–3085.
- (108) Shiraishi, Y.; Kanazawa, S.; Sugano, Y.; Tsukamoto, D.; Sakamoto, H.; Ichikawa, S.; Hirai, T. Highly selective production of hydrogen peroxide on graphitic carbon nitride  $(g-C_3N_4)$  photocatalyst activated by visible light. *ACS Catal.* **2014**, *4* (3), 774–780.
- (109) Drinking water: Past, present, and future. *EPA 816-F-00-002*; Office of Water, U.S. Environmental Protection Agency: Washington, DC, 2000.
- (110) Drinking water and ground water statistics, fiscal year 2011. *HERO* 2533123; Office of Water, U.S. Environmental Protection Agency: Washington, DC, 2013.